Chaudhari *et al*. *Energy Mater*. **2025**, *5*, 500082
DOI: 10.20517/energymater.2024.229

Energy Materials

Article

Open Access

Conductivity boosted $BiVO_4$ for enhanced OER and supercapacitive performance: stability insights with modeling, predictions, and forecasting using machine learning technique

Sagar A. Chaudhari[1], Vinod V. Patil[1], Vishal A. Jadhav[1], Parth Thorat[2], Santosh S. Sutar[2], Tukaram D. Dongale[3,4], Vinayak Parale[5], Vaishali Patil[6], Dattakumar S. Mhamane[7,*], Mukund G. Mali[1,5,*], Hyung-Ho Park[5,*]

[1]School of Chemical Sciences, Punyashlok Ahilyadevi Holkar Solapur University, Solapur 413255, India.
[2]Yashwantrao Chavan School of Rural Development, Shivaji University, Kolhapur 416004, India.
[3]Computational Electronics and Nanoscience Research Laboratory, School of Nanoscience and Biotechnology, Shivaji University, Kolhapur 416004, India.
[4]Functional Materials and Materials Chemistry Laboratory, Department of Physiology, Saveetha Dental College & Hospitals, Saveetha Institute of Medical & Technical Sciences, Saveetha University, Chennai 600077, India.
[5]Department of Materials Science and Engineering, Yonsei University, Seoul 03722, Republic of Korea.
[6]Department of Engineering Sciences and Humanities, Vishwakarma Institute of Technology, Pune, Maharashtra 411048, India.
[7]Department of Chemistry, Sangameshwar College (Autonomous), Solapur 413001, India.

[*]**Correspondence to:** Prof. Hyung-Ho Park, Department of Materials Science and Engineering, Yonsei University, 50 Yonsei-ro, Seodaemun-gu, Seoul 03722, Republic of Korea. E-mail: hhpark@yosei.ac.kr, Dr. Mukund G. Mali, School of Chemical Sciences, Punyashlok Ahilyadevi Holkar Solapur University, Solapur-Pune National Highway, Kegaon, Solapur 413255, India. E-mail: mukundgmali@gmail.com; Dr. Dattakumar S. Mhamane, Department of Chemistry, Sangameshwar College (Autonomous), Solapur, 165, Railway Lines, Saat Rasta, Solapur 413001, India. E-mail: dkumar.mhamane@gmail.com

How to cite this article: Chaudhari, S. A.; Patil, V. V.; Jadhav, V. A.; Thorat, P.; Sutar, S. S.; Dongale, T. D.; Parale, V.; Patil, V.; Mhamane, D. S.; Mali, M. G.; Park, H. H. Conductivity boosted $BiVO_4$ for enhanced OER and supercapacitive performance: stability insights with modeling, predictions, and forecasting using machine learning technique. *Energy Mater.* **2025**, *5*, 500082. https://dx.doi.org/10.20517/energymater.2024.229

Received: 29 Oct 2024 **First Decision:** 29 Nov 2024 **Revised:** 10 Dec 2024 **Accepted:** 26 Dec 2024 **Published:** 18 Apr 2025

Academic Editors: Jiazhao Wang, Xili Tong **Copy Editor:** Ping Zhang **Production Editor:** Ping Zhang

Abstract

To overcome the inherent limitations in the energy generation and storage properties of transition metal-based catalysts, it is crucial to develop processes that produce catalytic materials with high performance and long-lasting effectiveness. Herein, we synthesized Metal-Organic Framework (MOF)-derived $BiVO_4$ by mixing two separately prepared MOFs of Bi and V using trimesic acid and terephthalic acid as linkers. The separately prepared monometallic MOFs were then mixed and carbonized in an inert atmosphere followed by oxidation in air which gives the sample $BiVO_4$ with carbon (BVC). The prepared BVC electrode showed the overpotential 364 mV for oxygen evolution reaction at the current density of 10 mA cm^{-2}. In addition, the obtained BVC supercapacitor possesses a high specific capacity of 134.17 mAh g^{-1} (483 C g^{-1}) at 1 mA cm^{-2} current density. The aqueous and solid-state symmetric supercapacitor devices were also fabricated and achieved specific capacitance of 160.9 F g^{-1} and 109.8 F g^{-1} at 1 mA cm^{-2} current density, respectively. Moreover, the Long Short-Term Memory-based machine learning technique was employed to model, predict, and forecast the chronoamperometric stability of MOF-derived BVC electrodes for oxygen evolution reaction applications, and the capacitive retention and Coulombic efficiency BVC electrodes. The exceptional performance of the BVC electrodes is attributed to their porous structure containing conducting carbon, which offers enhanced conductivity, larger surface area and increased reactive sites for efficient electronic and ionic transfer. This novel approach to the synthesis of MOF-derived BVC has opened up new pathways for future energy storage and conversion.

Keywords: Metal-organic framework, monometallic, multifunctional, oxygen evolution reaction, supercapacitor, machine learning

INTRODUCTION

Nowadays, a society without portable electronic devices is inconceivable, as these devices have significantly modernized the way of living by making tasks easier and faster. In recent times, the rapid upsurge in the use of such electronic devices in daily life has ignited the development of efficient and portable, environment-friendly, and affordable energy conversion and storage devices[1-4]. These advancements have motivated researchers to create innovative, long-lasting technologies for energy conversion, such as water splitting for producing green hydrogen (H_2) fuel, and energy storage solutions such as lithium-ion batteries (LIBs) and supercapacitors (SCs)[5,6]. Amongst the energy storage technologies, SCs are the most promising storage devices to be developed for the present and future because of their long life cycles, long charge-discharge cycles, high power and energy densities, environment-friendly features, and safety reliability with low maintenance cost[7-9]. Although SCs have these advantageous characteristics, their low energy density has made them far less practical to use than batteries. Therefore, to fulfill future energy demands, it is imperative to increase the energy density of SCs using effective synthesis techniques[10,11]. On the other hand, amongst energy conversion technologies, hydrogen production through the electrocatalytic water splitting technique via oxygen evolution reaction (OER) or water oxidation is one of the supreme substitute green fuels. OER is a key component of the water splitting technique as it is a zero-emission route and presently is a crucial topic. In OER, molecular oxygen (O_2) is produced by coupled electron/proton reactions in acidic and basic environments[12]. Two H_2O molecules can be oxidized in an acidic environment to yield four H^+ ions and a O_2. On the other hand, four hydroxyl ions are oxidized and transformed into O_2 and water (H_2O) in an alkaline media. OER in an alkaline medium is more promising than in an acidic medium[13]. The half-cell reactions involved in basic conditions are as follows.

$$4OH^- \leftrightarrow O_2 + 2H_2O + 4e^- \qquad (1)$$

Due to the energy required at every step, the OER kinetics are sluggish, leading to a high overpotential. Noble metal-based materials are reported as high-performing electrocatalysts, but their scarcity and high cost limit them from being used as commercial catalysts[14]. Therefore, to overcome both the above-mentioned issues, stable, economical, highly abundant, and robust multifunctional electrocatalytic materials with a minimized overpotential of tetra-electronic water oxidation reaction (eq. 1) and high energy density especially at high power densities need to be developed[15].

Recently, a diverse range of materials based on Metal-Organic Frameworks (MOFs) have been developed and investigated for various electrochemical applications including LIBs[16,17], SCs[18], electrocatalytic hydrogen evolution reaction[19], OER[20], owing to their attractive features including high surface area, highly porous framework, and well-defined metal-ligand arrangement offering more active sites to make them the most promising candidates for electrochemical applications[21]. Furthermore, due to the synthetic tunability, MOFs serve as an ideal template material and precursor to develop carbon matrix incorporated metallic nanomaterials on pyrolysis under an inert atmosphere. These materials have carbon matrices with metal nanomaterials offering extra accessibility of active sites to an electrolyte, resulting in a larger contact area between them which proved to be crucial behind enhanced electronic properties[22,23]. Recently, extensive work has been undertaken focusing on the development of non-noble mono-/bi-metallic MOF-derived metal oxides, sulfides, phosphides, etc. and used to fabricate working electrodes in SC and OER/hydrogen evolution reaction (HER) applications[24]. Lately, $BiVO_4$ (BV) has gained attention in electrochemical and electrocatalytic OER applications due to its excellent physic-chemical properties and stability. However, pristine BV was found to show poor electronic conductivity which could adversely affect the capacitive retention (CR) of SC devices and the rate of a water oxidation reaction in OER. One of the best remedies to minimize this problem is to adopt a MOF-derived synthesis of BV, in which calcination of Bi-MOF precursor in the presence of suitable vanadium salt produces BV/C composite having larger surface area, better conductivity, and more number of surface active sites than bare BV. There are very few reports based on this approach to BV synthesis and its use in SC and OER applications[25].

In response to the above-mentioned concerns, herein, for the first time, we report the unique solid-state approach to synthesizing MOF-derived bismuth vanadate/carbon (BVC) composite by mechanically mixing the separately prepared monometallic Bi-MOF (using trimesic acid as a linker) and V-MOF (using terephthalic acid as a linker) precursors. In this study, rather than following the traditional method (where Bi-MOF and vanadium metal salt serve as precursors to synthesize the BVC catalysts), we opted to utilize separately prepared monometallic Bi-MOF (CAU-17) and V-MOF (MIL-47) as the Bi and V precursors. The rationale behind utilizing the two different linkers is their distinct coordination properties with respective metal nodes, i.e., Bi and V. With this approach, it is possible to achieve tailored properties with controlled morphology while mitigating the common challenges of uneven metal distribution and agglomeration typically observed in bimetallic MOFs[26]. This alternative approach is expected to further improve the catalytic properties of BVC as the use of two different linkers with different sp^2 characters could improve specific surface area and electronic conductivity considerably which in turn decide the number of surface active sites. The use of two monometallic MOFs instead of bimetallic MOFs to synthesize bimetallic oxide materials is proven to be efficient in developing high-performance catalytic activity materials[26]. The desired structure was confirmed through several structural and morphological spectroscopic characterizations of the prepared BVC electrode. This was subsequently compared with a pristine BV sample, both of which were then subjected to SC and OER tests. The stability of the electrodes was also measured and analyzed by using a Long Short-Term Memory (LSTM)-based machine learning approach. The CR and Coulombic efficiency (CE) of BV and BVC SC electrodes were modeled, predicted and forecasted using this technique. Such a modeling approach opens new avenues to predict and forecast the critical parameters of the energy devices[27].

EXPERIMENTAL

Materials and reagents

Bismuth (III) nitrate pentahydrate [$Bi(NO_3)_3 5H_2O$, Alfa Aesar], Vanadium (III)chloride (VCl_3, Sigma Aldrich), Benzene-1,3,5-tricarboxylic acid (H_3BTC, Sigma Aldrich), Benzene-1,4-dicarboxylic acid (H_2BDC, Sigma Aldrich), Potassium hydroxide (KOH, SD Fine), Methanol (CH_3OH, Spectrochem), and N, N-Dimethylformamide (C_3H_7NO, Spectrochem) were used. All reagents were of analytical purity grade and used without further purification. Distilled water was used thoroughly.

Synthesis of CAU-17 (Bi-MOF)

To prepare Bismuth MOF (CAU-17), the 0.454 gm of $Bi(NO_3)_3$ $5H_2O$ and 0.957 gm of H_3BTC were separately dissolved in a 30 mL mixture (1:1 V/V) of methanol and N, N-Dimethylformamide. The metal salt solution was then slowly added to the H_3BTC solution and stirred for 15 min and then transferred into a 100 mL Teflon-lined stainless steel (SS) autoclave and heated at 120 °C for 24 h. The reaction mixture was allowed to cool at room temperature and the obtained product was collected by centrifugation followed by washing with methanol. The washed product was dried at 80°C overnight to obtain Bi-MOF.

Synthesis of MIL-47 (V-MOF)

To synthesize Vanadium MOF (MIL-47), 0.664 gm of H_2BDC was dissolved in 50 mL N, N-Dimethylformamide and stirred until a clear solution was obtained. Once the solution was clear, it was placed in the dark, and 0.628 gm of VCl_3 was added. The mixture was stirred for 30 min and ultrasonicated for 15 min in the dark (since VCl_3 oxidizes under light). The solution was then transferred into a 100 mL Teflon-lined SS autoclave and heated at 120 °C for 48 h, after which it was allowed to cool to room temperature. The obtained greenish product was collected by centrifugation at 4000 rpm, washed first with DMF then twice with methanol, and dried at 60 °C for 12 h.

Synthesis of BV and BVC

The BV was synthesized by using obtained products from MOFs as a precursor for synthesis by mixing 1:1 (weight ratio) Bi-MOF and V-MOF, respectively, and grinding them in a mortar pestle for 15 min. This mixture was collected into a quartz crucible incorporated in a horizontal quartz tube furnace. The furnace was heated at a ramping rate of 4 °C/min until it reached a final temperature of 450 °C, where it was maintained for 120 min in air atmosphere and then allowed to cool naturally. BVC was synthesized by heating the Bi-MOF and V-MOF (1:1 weight ratio) mixture in an argon atmosphere at 700 °C for 150 min, followed by calcination to 400 °C for 120 min in the air at a ramping rate of 4 °C/min. Scheme 1 displays a schematic illustration of all the steps involved in BV and BVC synthesis.

RESULTS AND DISCUSSION

Structural and morphological study

All the details on the instrumentation used for the physicochemical characterizations are provided in Supplementary Section 1.1. The phase formed and its crystal structure are characterized by X-ray diffraction (XRD) spectroscopy, as shown in Figure 1A. The diffraction peaks at 2θ 18.83°, 28.85°, 30.43°, 34.51°, 35.32°, 39.91°, 42.40°, 46.36°,47.05°, 50.12°, 53.35°, 55.70°, 58.46° and 59.23° corresponded to the (110), (121), (040), (200), (020), (211), (150), (132), (240), (202), (161), (215), (321) and (123) planes, respectively.

The crystalline monoclinic phase of BV and BVC was confirmed as all the peaks are in line with the planes of the JCPDS card No.14-0688[28,29]. No any distinct peak was observed in the XRD spectrum of BV and BVC due to minimal amount of carbon in BVC, but the hump from 15°-30° evidenced the presence of an amorphous carbon matrix. Interestingly, a slight shift in the peaks toward higher 2θ values was observed with the addition of carbon compared to pure bismuth vanadate. The peak along the (110) plane reveals an approximate 0.03° shift, confirming the effective incorporation of carbon in BV lattice. This peak shift in the case of BVC is due to stress and strain induced by the carbon via creating minor defects or distortion in BVC without damaging the overall structure. This shift evidences the intimate interaction between BV and carbon, thereby confirming the successful formation of the BVC composite. Additionally, the peak intensity of the BVC sample decreased with the carbon incorporation, compared to pristine BV. This decrease in intensity is attributed to local structural inhomogeneity, resulting in reduced crystallization. The crystallite

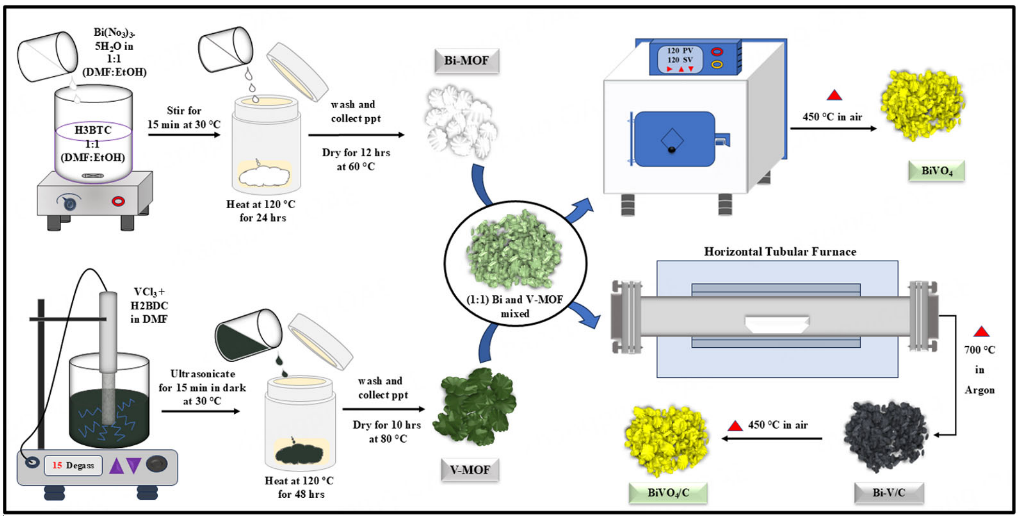

Scheme 1. Schematic illustration on synthesis of BV and BVC. BV: $BiVO_4$; BVC: bismuth vanadate/carbon; MOF: metal-organic framework.

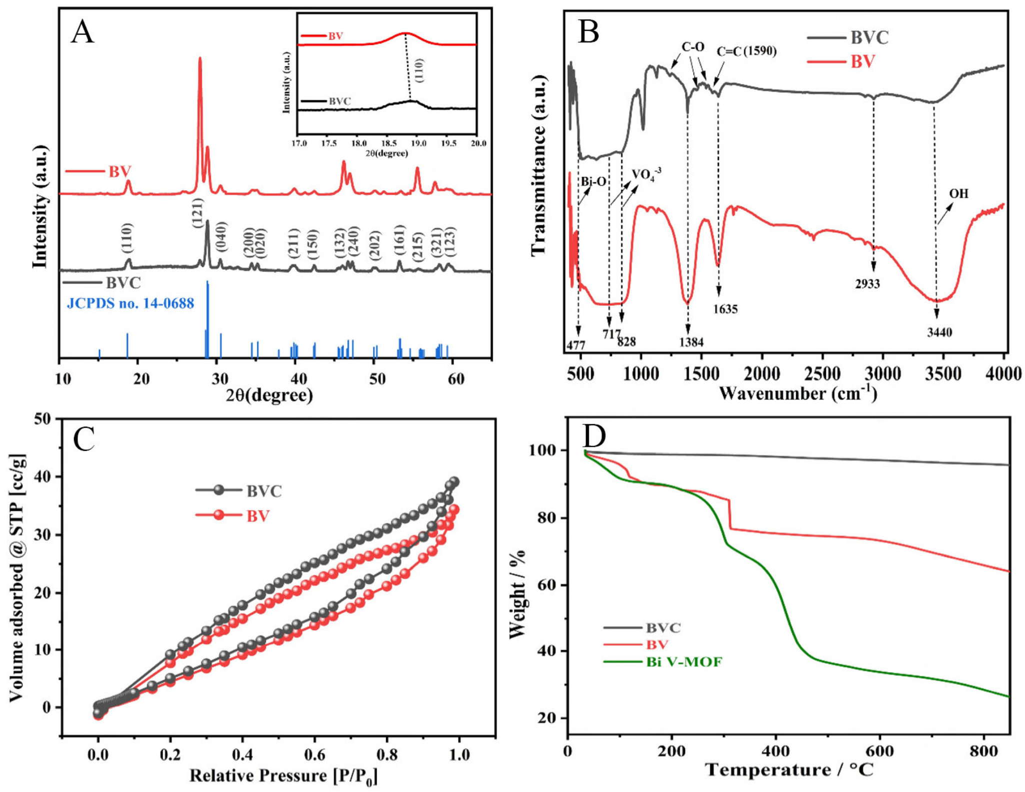

Figure 1. (A) X-ray diffraction patterns of the BV and BVC samples and the inset shows the (110) plane shifting; (B) The FTIR plots of BV and BVC; (C) N_2 adsorption-desorption isotherms for BV and BVC (D) TGA of Bi V-MOF, BV, and BVC samples. BV: $BiVO_4$; BVC: bismuth vanadate/carbon; FTIR: fourier-transform infrared spectroscopy; TGA: thermogravimetric analysis; MOF: metal-organic framework.

size was determined using the full width at half maximum (FWHM) of the peak along the plane (110). In the case of the BV sample, the FWHM was 0.5401, while for the BVC sample, it was 0.5969 and the values are provided in Supplementary Table 1. Based on these FWHM values, the crystallite sizes were calculated using the Scherrer Supplementary Equation 1 yielding 14.908 nm for the BV sample and 13.489 nm for the BVC sample. Furthermore, the dislocations are one-dimensional crystalline defects that define the boundary between slipped and unslipped regions within a material. These defects disrupt the regular atomic arrangement found in a perfect crystal. The extent of defects in the material is quantified by a measure known as dislocation density (ρD). The ρD refers to the number of dislocations per unit volume of crystalline material. A smaller ρD combined with larger grain sizes indicates a more crystallization process and the larger ρD combined with smaller grain sizes indicates a more amorphization process[30]. The term microstrain (ε) is defined as the deformation of an object divided by its effective length. The ε and ρD were calculated using Supplementary Equations 2 and 3. The ε and ρD for the BV sample were 14.235×10^{-3} nm^2 and 4.499×10^{-3} nm^2, respectively. With the addition of carbon to BV, these values increased to 15.708×10^{-3} nm^2 and 5.495×10^{-3} nm^2 for the BVC sample. As shown in Supplementary Figure 1 plotting the broadening of diffraction peaks against the sine of the diffraction angle, the Williamson-Hall (W-H) plot is a useful technique for evaluating XRD data since it enables the measurement of required crystallite size and ε. This method facilitates a thorough understanding of the structural properties of the materials by revealing a linear connection in which the intercept gives information about crystallite size and the slope corresponds to the ε. Also, by using W-H plots [Supplementary Figure 1], the required crystallite size and strain were calculated using Supplementary Equation 4. The values for the BV sample were 0.0000410 and 16.197, respectively, enhanced to 0.0036 and 42.662 with the incorporation of carbon (BVC), as shown in Supplementary Table 1.

The prepared samples were characterized by using Fourier-transform infrared spectroscopy (FTIR), as shown in Figure 1B. The peak at 477 cm^{-1} is of Bi-O and 717 cm^{-1} and 828 cm^{-1} for V-O in VO_4^{-3} confirming the synthesis of BV monoclinic phase in both BV and BVC samples[31,32]. The bands at 1,384 cm^{-1} and 1,635 cm^{-1} are due to C-O and C=O bonds due to the adsorption of atmospheric carbon dioxide during the synthesis. The peak at 1,590 cm^{-1} for C=C observed in only BVC evidences the presence of carbon in the sample. In addition, the BVC has numerous oxygen-holding groups from (1200-1620) which were absent in BC confirms the presence of carbon in MOF-derived BV. The broad peaks at 2,933 and 3,440 cm^{-1} are due to the stretching and bending vibration modes of the -OH group of atmospheric water molecules adsorb on the surface of the catalyst[26,33,34].

The surface area of BVC and BV were recorded using Brunauer-Emmett-Teller surface (S_{BET}) analysis, as shown in Figure 1C. The obtained surface area of BVC and BV were found to be 26.839 m^2/g and 24.732 m^2/g as both the samples show N_2 absorption isotherm narrow H3-type loop with a type-IV hysteresis curve, confirming the mesoporous nature of the samples[35]. Barrett-Joyner-Halenda (BJH) method was used to calculate the pore size from desorption isotherms. The pore volume of BVC was 0.058 cc/g and that of BV was 0.052 cc/g; the pore diameters of BVC and BV were 3.51 nm and 3.13 nm, respectively. The greater surface area of BVC is attributed to the conducting sp^2 carbon incorporated *in-situ* potentially providing extra active sites for electrocatalytic ion transfer and storage.

The thermogravimetric analysis (TGA) of Bi V-MOF, BV, and BVC is shown in Figure 1D. Four weight loss processes are observed for Bi V-MOF. The first occurs from room temperature to 122 °C, primarily due to the elimination of coordinated water molecules. The second, from 122 °C to 300 °C, is attributed to the removal of volatile organic compounds. The third, from 300 °C to 465 °C, corresponds to the disintegration of the framework in the sample. The fourth, from 465 °C onwards, involves the complete oxidation of carbon residues and the oxidation of MOFs. The BV sample showed weight loss of up to 125 °C due to dehydration and removal of volatile organic compounds up to 310 °C from 310 °C; the peak drop is attributed to the quick change in phase of the material and the crystallization of material takes place. The BVC sample showed negligible weight loss (approximately 5%) beyond 465 °C due to the loss of carbon remaining after carbonization at 700 °C, confirming the presence of carbon in the BVC[26].

Field Emission-Scanning Electron Microscopy (FE-SEM) was used to determine the morphology of the prepared samples. Figure 2 displays FE-SEM images of BVC and BV. The uneven distribution of the BV nanoparticles and agglomeration can be seen in Figure 2A and B. Figure 2C and D shows the micrographs of BVC and the uniformly distributed coral-like nanoparticles. Additionally, the diffusion length can be greatly shortened by the cavities and gaps created by uniformly distributed coral-like nanoparticles, facilitating easy ion intercalation across the material[36]. For the BV and BVC samples, the average particle size was determined and noted in histograms, and the average particle diameter was determined to be around 107 nm, and 75 nm, respectively, as shown in Figure 2E and F. The obtained results demonstrate that the incorporation of carbon affects the materials morphology and structure, which may further influence the electrochemical performance. The elemental mapping of BVC is shown in Figure 2G-K representing Bi, V, O, and C elements, respectively. The elemental mapping has confirmed the presence of doped carbon in the lattice of BV nanoparticles.

To support the FE-SEM and morphology, the BV and BVC samples were further investigated using the High-Resolution Transmission Electron Microscopy (HRTEM) technique. HRTEM images of BV at low and high magnifications show the nanoparticle-like morphology in Figure 3A. It is possible to clearly identify the lattice fringes of BV nanoparticles from the higher-resolution magnified image [Figure 3B and C]. The lattice d-spacing of 0.311 nm was derived from the lattice fringes, which corresponded to the (121) plane of the BV and BVC at 28.85° nanoparticles. Likewise, HRTEM was used to examine the BVC material, as displayed in Figure 3D-F at various magnifications. It was illustrated that the BVC coral-like nanoparticles are irregularly arranged, with carbon nanoparticles positioned in between them. Furthermore, Figure 3F makes it easy to identify the lattice fringes associated with the BV nanoparticles in the BVC material. Based on the lattice fringes, the BVC coral-like nanoparticles (121) plane is represented by the measured interplanar spacing of 0.306 nm. According to the findings, the BVC d-values from the XRD pattern were likewise well-coordinated with HRTEM results[37,38].

The surface properties of the synthesized materials such as elemental composition and their bonding states (oxidation states) were studied by X-ray photoelectron spectroscopy (XPS) [Figure 4]. The survey spectrum of BV and BVC samples displays the peaks of each element present in the samples. The presence of Bismuth (4f), Vanadium (2p), Oxygen (1s), and Carbon (1s) at their respective positions of binding energy (BE) is confirmed by XPS survey spectra presented in Supplementary Figure 2. Figure 4A is the high-resolution XPS spectra of Bi 4f of BV and BVC samples showing two broad peaks of Bi^{3+}. The BEs of 164.4 eV and 164.28 eV represent Bi $4f_{5/2}$, while 159.09 eV and 158.98 eV correspond to Bi $4f_{7/2}$, respectively. The difference between the BEs of both peaks agrees well with pure BV. The high-resolution XPS-spectra of V 2p [Figure 4B] were fitted into two peaks of V $2p_{3/2}$ and V $2p_{1/2}$ at the BEs of 517 eV and 524.3 eV for BV and 516.7 eV and 524 eV for BVC. The V $2p_{3/2}$ deconvoluted into two distinct peaks at the BE of 517 eV and 515.8 eV and 516.7 eV and 515.3 eV for BV and BVC, respectively, representing the presence of V^{5+} and V^{4+}. Figure 4C represents the high-resolution spectra of O 1s which was fitted into three peaks at the BE 529.9 eV, 531 eV, and 532.7 eV for BV and 529.7 eV, 530.7 eV and 532.6 eV for BVC indexed for metal-oxygen bonds (Bi-O or V-O bonds), the hydroxide or crystal defects and the chemisorbed oxygen or surface adsorbed oxygen, respectively. Figure 4D represents the C 1s deconvoluted into two peaks at BEs of 284.6 eV, 285.6 eV for BV and 284.5 eV, 285.5 eV for BVC representing the C-C and C-O bonds, respectively. Additionally, the lower intensity of C 1s in BV than in BVC confirms the presence of

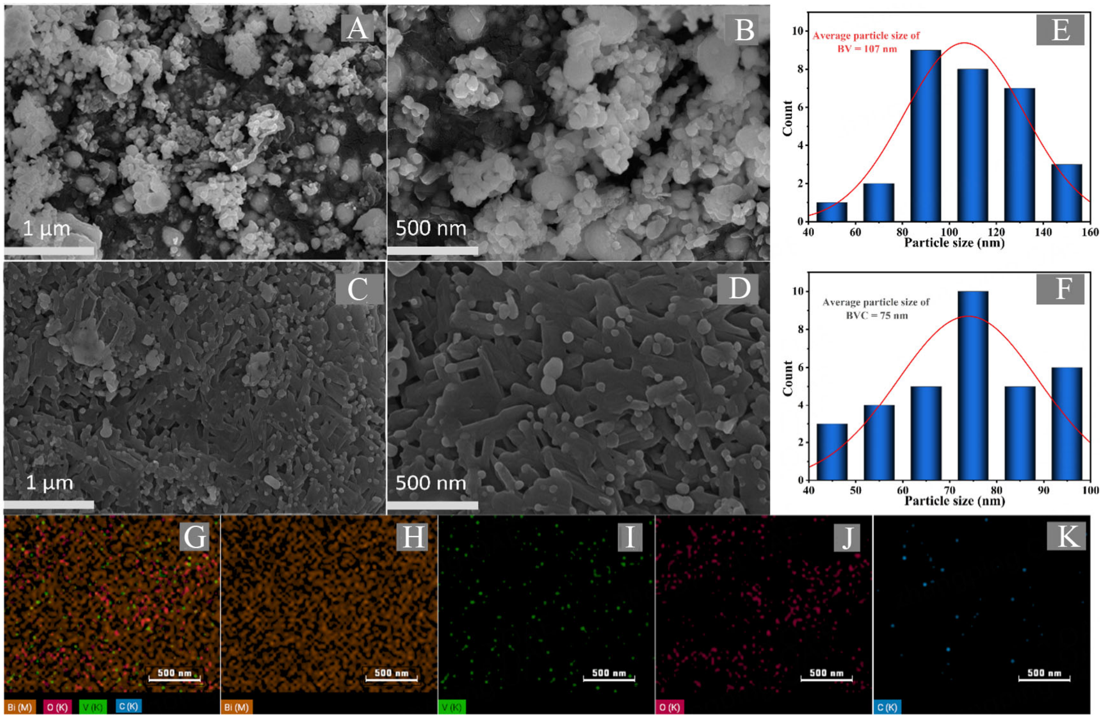

Figure 2. FE-SEM images of (A and B) BV; (C and D) FESEM of BVC; (E) Histogram for average particle size of BV; (F) Histogram for average particle size of BVC, and the elemental mapping of BVC sample with, (G) overlay, (H) Bi, (I) V, (J) O, and (K) C elements. BV: $BiVO_4$; BVC: bismuth vanadate/carbon; FE-SEM: field emission-scanning electron microscopy.

conductive sp2 type of carbon in BVC[39]. The shifting of Bi 4f, V 2p, C 1s, and O 1s of the BVC sample to the lower BE in comparison to their initial locations in BV was due to the presence of oxygen vacancies[40]. The presence of a higher amount of surface oxygen vacancies in BVC than in BV is expected to improve charge transfer properties to achieve better electrocatalytic performance[41-43].

Oxygen evolution reaction study

The electrocatalytic OER performance of the prepared catalyst was studied in 1M KOH solution. The standard three-electrode system was used for testing the electrodes and the details of electrochemical measurements are provided in Supplementary Section 1.2. Figure 5A represents the linear sweep voltammetry (LSV) at 1 mV s^{-1} of BVC and BV. The thermodynamic potential for water splitting is 1.23 V *vs.* reversible hydrogen electrode (RHE); the active OER catalyst should attain this potential at a 10 mA cm^{-2} current density[44]. The measured voltages were converted from Hg/HgO to the RHE scale using the Nernst Supplementary Equation 5. The overpotential (η_{10}) calculated using Supplementary Equation 6 required to reach the current density of 10 mA cm^{-2} for MOF-derived BVC is 364 mV, which is much lesser than the 432 mV observed for BV. This indicates that BV alone has limited performance, but its efficiency and stability are significantly improved when modified with MOF-derived doped carbon.

Figure 5B shows the Tafel slopes obtained from LSV curves, calculated using Supplementary Equation 7. BVC exhibits a lower Tafel slope of 51 mV dec^{-1}, while BV shows a Tafel slope of 61 mV dec^{-1}. The lower overpotential and Tafel slope indicate that BVC showcases better OER activity than BV. Moreover, in Figure 5C, electrochemical conductivity studies were conducted at an open circuit voltage employing electrochemical impedance spectroscopy (EIS) to examine their intrinsic transport properties. The equivalent circuit was developed by fitting the matched data. Each electrode shows discrete semicircles at

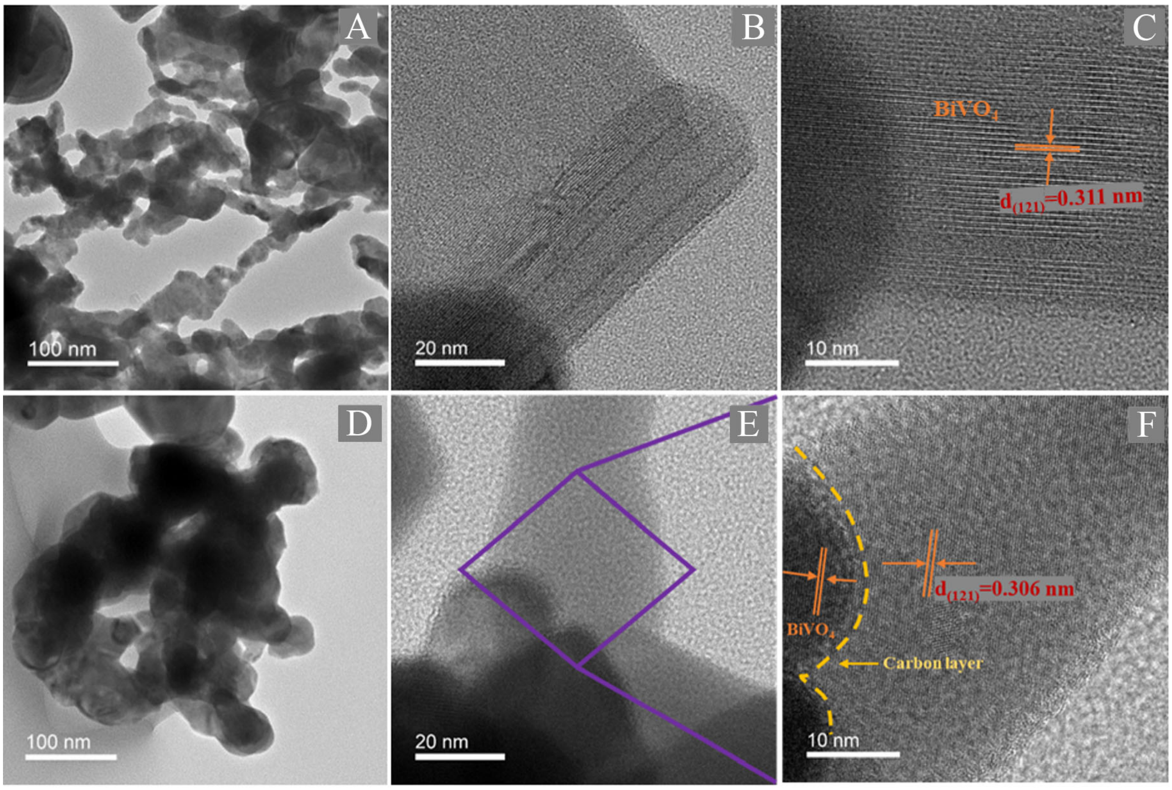

Figure 3. HRTEM of (A-C) BV, and (D-F) BVC samples. BV: BiVO$_4$; BVC: bismuth vanadate/carbon; HRTEM: high-resolution transmission electron microscopy.

high frequencies and a straight line at low frequencies. A semicircle radius is assigned to the charge-transfer resistance (R_{ct}) in the electrochemical process between the electrolyte and the electrode. The smaller radius of the semicircle points to a lower R_{ct} and a higher electron transfer rate. The curve's intercept at the real axis or its starting point in the high-frequency region corresponds to the solution resistance (R_s). The Warburg impedance (R_w) values, which offer insights into the ion diffusion process, and the constant phase element (CPE) values, which detail the active interface of the electrodes, are presented in Supplementary Table 2. R_s is the intercept on the horizontal axis containing electrolyte resistance, contact resistance among the current collector and the active substances, and internal electrode resistance. The quasi-semicircle signifies the R_{ct} determined by the electrostatic interactions and faradic redox process, which proceeds at the electrode and electrolyte interface. The slope of the straight line specifies R_w, signifying the charge diffusion kinetics process within the active material. The lower values of R_s and R_{ct} of BVC (0.018 Ω and 0.5 Ω) compared to those of BV (0.003 Ω and 0.8 Ω) clearly confirm the accelerated charge transfer process in BVC, resulting in superior OER activity.

The electrochemical double-layer capacitance (C_{dl}) of the electrodes was calculated using cyclic voltammetry (CV) in a non-Faradic region of 0.924 V to 1.22 V *vs.* RHE. The CV curves were obtained from 10-100 mV s^{-1} scan rates in 1M KOH aqueous solution. Figure 5D and E shows CV curves of BV and BVC; the scan rate determines the double-layer charging current, and possibly, the C_{dl} values were determined from the slope of a liner connection. Electrochemical C_{dl} was calculated from Supplementary Equation 8, as displayed in Figure 5F. The BV and BVC show C_{dl} values of 0.696 mF cm^{-2} and 0.762 mF cm^{-2}, respectively. The electrochemical active surface area (ECSA) of BV and BVC is determined by Supplementary Equation 9 ; it can serve as a reliable indicator to determine if any substantial changes have taken place at the electrode

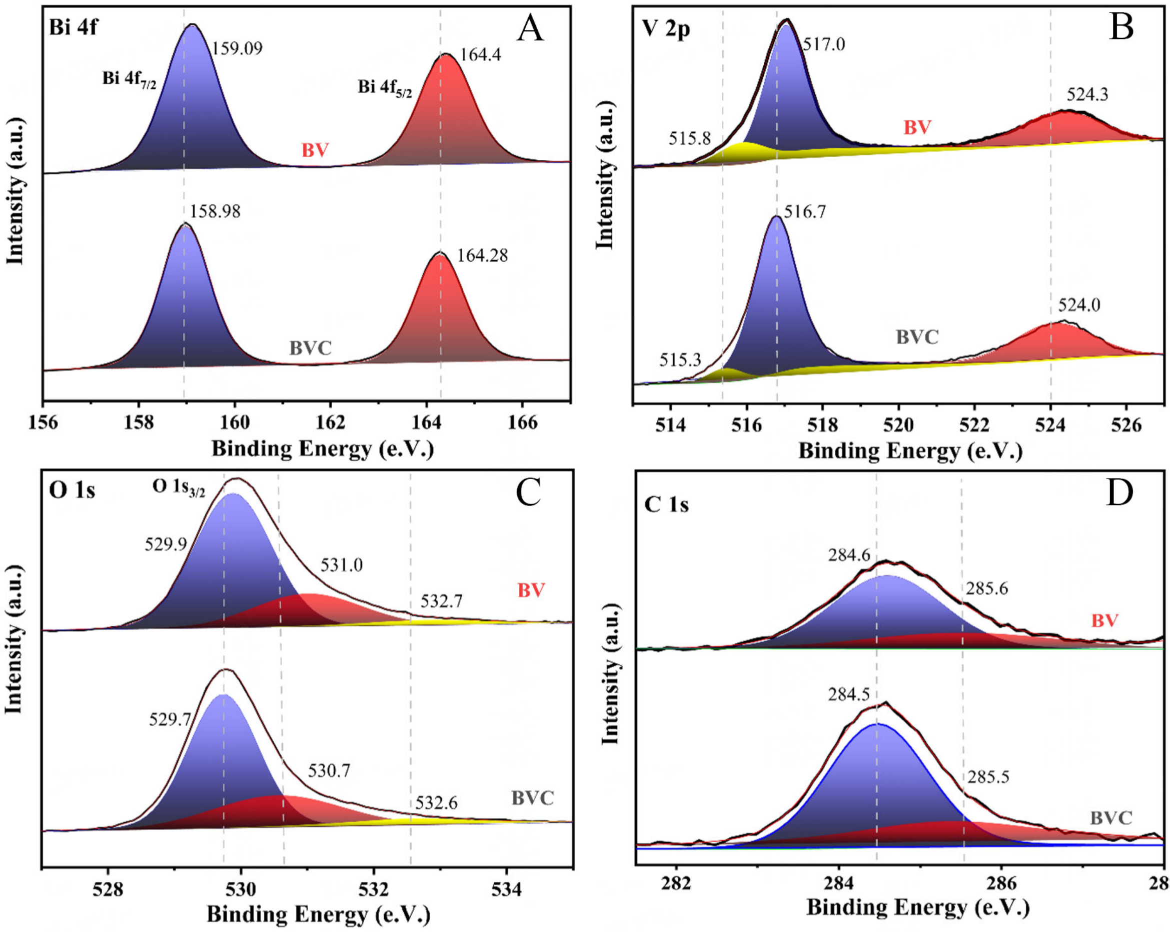

Figure 4. XPS spectra of BV and BVC for (A) Bi 4f, (B) V 2p, (C) O 1s, and (D) C1s. BV: $BiVO_4$; BVC: bismuth vanadate/carbon; XPS: X-ray photoelectron spectroscopy.

contact. The increase in ECSA values indicates enhanced electrocatalytic activity in the material due to increased surface area and greater exposure of catalytic sites during electrocatalysis. Here, BV and BVC give the ECSAs of 17.4 cm^2 and 19.05 cm^2, indicating the superior performance of BVC over BV. The roughness factor (RF) is calculated using Supplementary Equation 10; the RF values were determined to be 17.4 and 19.05 for BV and BVC, respectively. The C_{dl}, ECSA, and RF values indicate that the BVC has additional active sites than the BV which gives excellent OER results. The stability of the material/electrode is very important for its use for longer durations. Therefore, we have tested the stability of the BVC sample for continuous oxygen evolution. Figure 5G shows a long-term chronoamperometry (CA) curve recorded for 12 h at a constant potential to supply a 10 mA cm^{-2} current density to guarantee the robustness and longevity of the catalyst. A virtually constant current shows exceptional stability of the catalyst material, and the initial increase in current density is associated with continuous material activation and effective interaction of the catalyst with the electrolyte. The stability of BVC is further analyzed using LSTM-based machine learning techniques to model and predict the time evolution behavior of current to understand the stability of OER. The results asserted that the LSTM can capture temporal trends and predict the current density values very well, suggesting the model's ability to predict the data accurately along with the forecast current density for next 150 min, also proving the stability of the catalyst [Figure 5G]. The mean squared error (MSE) between experimental and predicted current densities was found to be very small (8×10^{-4}), showcasing the successful prediction. Figure 5H displays the LSV polarization curve of BVC, which shows

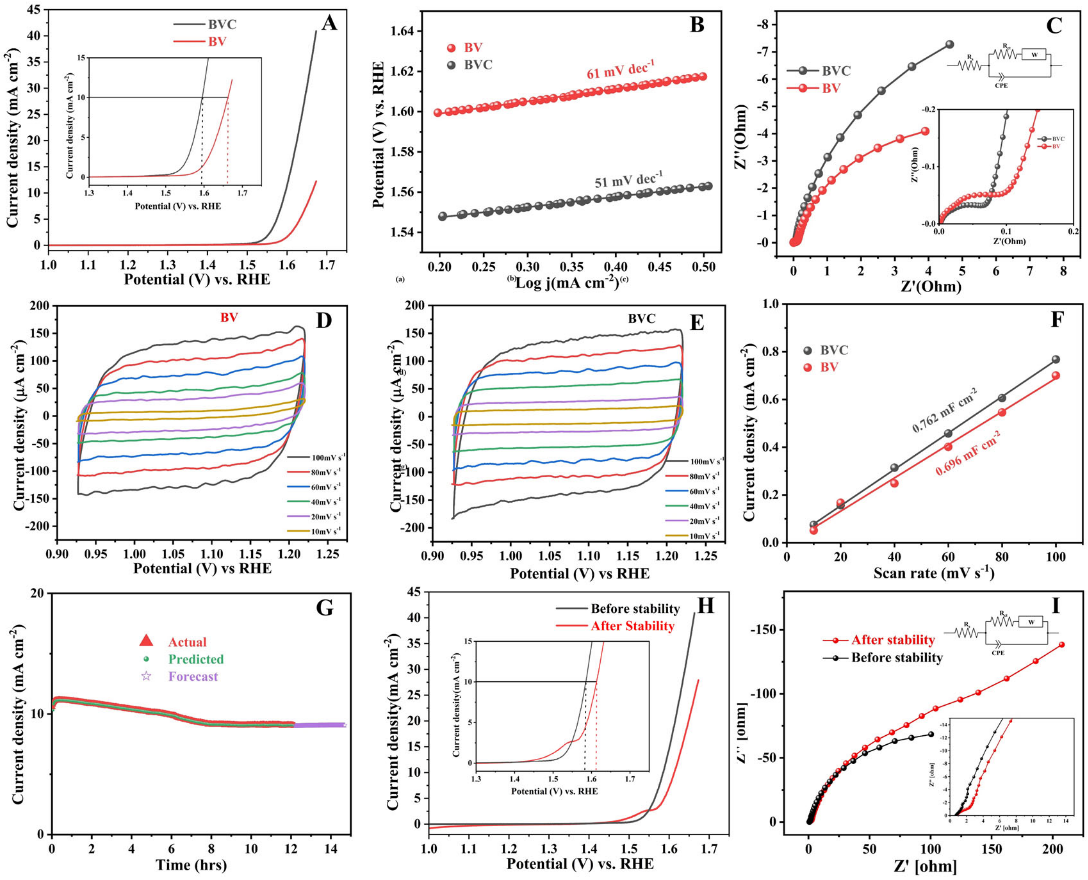

Figure 5. (A) Linear sweep voltammetry (LSV) curves of as-prepared catalysts BV and BVC electrodes; (B) Corresponding Tafel slopes; (C) EIS Nyquist plots 1 MHz to 10 mHz; (D and E) Cyclic voltammograms of BV and BVC; (F) Current density with respect to scan rates of BV and BVC electrodes, i.e., double layered capacitance (C_{dl}); (G) The actual, predicted, and forecasted chronoamperometry (CA) curve of BVC in 1.0 M KOH; (H) LSV curves for OER measured before and after CA stability at 1 mV s^{-1} scan rate; (I) EIS Nyquist plots of the electrode before and after the stability test. BV: $BiVO_4$; BVC: bismuth vanadate/carbon; OER: oxygen evolution reaction.

an initial overpotential of 1.59 V *vs.* RHE and, after 12 h, shows an overpotential of 1.61 V *vs.* RHE at the current density of 10 mA cm^{-2}. This performance confirms minimal current decay for the period of 12 h, demonstrating the high durability and stability of the catalyst. The EIS Nyquist plots in Figure 5I showed a negligible increase in resistance, confirming the charge transfer rate; therefore, OER performance remains unaffected over longer durations. The OER mechanism and actual evolution of oxygen gas for the BVC sample using a three-electrode setup are demonstrated in Supplementary Video 1.

Supercapacitor study

Electrochemical performance evaluation of BV and BVC electrodes

The electrochemical characteristics of the BVC and BV electrodes were investigated using CV, Galvanostatic Charge Discharge (GCD), and EIS. The three-electrode system was used, with BVC and BV as the working electrodes, a platinum wire as a counter electrode, and Hg/HgO as a reference electrode. The CV measurements of BV and BVC at scan rates from 100 mV s^{-1} to 10 mV s^{-1} in the potential window of 0 V to -1.0 V *vs.* Hg/HgO were measured in 1 M KOH as an electrolyte. In Figure 6A and B, the CV curves of both BV and BVC showing the oxidation and reduction peaks can be attributed to the reversible faradic process $Bi^{+3} \leftrightarrow Bi^0$. The only reduction peak from -0.7 V to -0.85 V was due to Bi^{3+} to Bi^0 and the couple of oxidation peaks from -0.5 V to -0.4 V and -0.375 to -0.275 were attributed to the Bi^0 to Bi^{1+} and Bi^{1+} to Bi^{3+}.

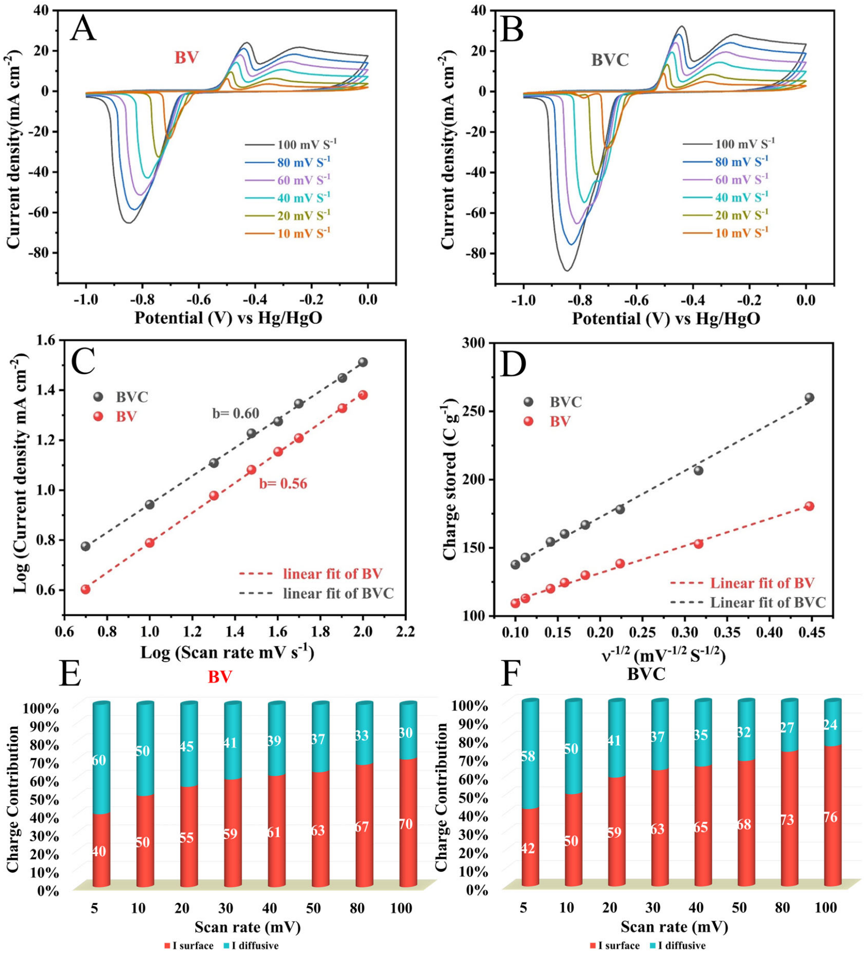

Figure 6. (A and B) Comparative CV curves of BV and BVC; (C) Plot of the log of current density *vs.* log of scan rate for BV and BVC electrodes to calculate the "b" values in CV curves; (D) The plot of charge stored *vs.* reciprocal of square root of potential scan rate of BV and BVC; (E and F) Comparison of the surface and diffusive charge contribution at scan rates (5-100 mV s^{-1}) in BV and BVC electrodes. BV: $BiVO_4$; BVC: bismuth vanadate/carbon; CV: cyclic voltammetry.

The shifting of oxidation peaks towards positive potential and the shifting of reduction peaks to negative potential are attributed to the internal resistance (IR) drop factor, observed from the 100 mV s^{-1} to 10 mV s^{-1} scan rates, respectively[45]. The nature of CV for BVC and BV is the same as the presence of the carbon provides a higher surface area and accommodates more electrolyte ions with quick migration. To gain a better understanding of the performance, the cyclic voltammograms (CVs) of the bare SS electrode and BVC were compared in Supplementary Figure 3A. Additionally, the composition of the electrodes, with respect to the active material, activated carbon and binder, was varied during electrode fabrication; the optimized performance was evaluated. The resulting CVs were recorded and compared in Supplementary Figure 3B. Hence, the higher current response observed in BVC results in a higher specific capacity compared to BV.

The redox nature reveals the pseudocapacitive electrical activity of electrodes. Subsequently, the capacitive contribution of BVC and BV electrodes was calculated using the Power law Supplementary Equations 11 and 12 to determine the charges stored by the surface (involving non-faradic reactions adsorption-desorption of charges) and/or the diffusion charge storage (bulk intercalation process) from the CV curves of BV and BVC electrodes. The contribution of charge storage is calculated from the constant b (slope of linear graph) by plotting the log of scan rate (mV s^{-1}) *vs.* log of current density line (A g^{-1}). The b value of ~1 indicates a surface control process (non-faradic) dominance, while a b value of ~0.5 represents a diffusion control process (faradic) dominance. The b values in Figure 6C of BV and BVC are 0.56 and 0.6, respectively, indicating that the BVC electrode exhibits both surface-controlled and diffusion-controlled processes.

The amount of charge stored in BV and BVC was quantified by the contribution of observed charge density (Q_t), calculated using the modified Powers law for the surface pseudocapacitive process (Q_s - $I_{surface}$) and battery-like diffusive process (Q_d - $I_{diffusive}$). Q_t is the total stored charge, Q_s is the surface stored charge related to electric double-layer capacitors (EDLCs), and Q_d is the diffusion stored charge, which occurs in the bulk. The Q_d and Q_s are dependent on the square root of the scan rate. To calculate the approximate values of Q_s and Q_d, the plot of total voltammetric charge (Q_t, charge stored in C g^{-1}) *vs.* the reciprocal square root of sweep rate is shown in Figure 6D. Supplementary Equations 13 and 14 were used to measure the contribution of Q_d and Q_s in total charge contribution. The proportion of $I_{surface}$ and $I_{difussive}$ charge stored contribution in BV and BVC is depicted in Figure 6E and F. The sky blue and red area represents the $I_{difussive}$ (bulk) and $I_{surface}$ (capacitive) charge storage contribution in the total current, respectively. The $I_{surface}$ (capacitive) contribution emerges with higher scan rates. The sample BVC has an $I_{surface}$ (capacitive) contribution of 76%, while BV has a contribution of 70% at 100 mV s^{-1}. This confirms the effective redox kinetics for BVC are enhanced as the *in-situ* carbon incorporation takes place.

The GCD curves of BV and BVC electrodes at different current densities from 1 to 5 mA cm^{-2} between the potential window of 0 V to -1.0 V were recorded and displayed in Figure 7A and B. These curves exhibited non-linear charge-discharge behavior, representing pseudocapacitive properties of BV. The performance, in terms of specific capacity, for BV and BVC was calculated using Supplementary Equations 15 and 16 from the GCD curves. The obtained specific capacities of BV and BVC are 45.14 mAh g^{-1} (162.5 C g^{-1}) and 134.17 mAh g^{-1} (483 C g^{-1}), respectively, at the current density of 1 mA cm^{-2}, showing almost a threefold rise in performance for BVC compared to BV. The literature reports on BV and their composites for SCs are compared in Supplementary Table 3. Figure 7C compares the GCD curves of BV and BVC at a current density of 1 mA cm^{-2}. This enhanced performance is credited to the *in-situ* MOF-derived carbon and the morphology which provides a high surface area and active sites for the high electronic, ionic transfer and storage during electrochemical analysis. Figure 7D shows the comparative graph of specific capacity *vs.* current density of BV and BVC samples. At elevated current densities, only the outside layer of electrode materials engages in the electrochemical process, resulting in decreased specific capacity. While at a lower current density, the electrochemical redox reaction occurred in bulk, giving a high specific capacity. The durability and applicability of electrodes are also the most significant aspects. The cyclic stability of the electrodes was tested for 2000 cycles, and their performance was predicted and forecasted using the LSTM-based machine learning technique to assess the material's efficiency and applicability. The dataset comprised stability data from 2000 cycles of CR and CE for BVC and BV electrodes, split into training (80%) and test (20%) sets. The LSTM model, optimized with a batch size of 5, sigmoid and tanh activation functions, and the Adam optimizer, was trained over 100 epochs. The hyperparameter tuning via grid search minimized MSE, enabling accurate predictions for CR and CE. This process ensures that the model delivers an accurate prediction for the CR and CE values of BVC and BV. The lower MSE values reflect the model's ability to predict the data accurately. The MSE values are summarized in Supplementary Table 4. The LSTM model has been accurately fitted to the actual data and is also able to forecast the CR and CE behavior of the electrodes for the next 500 cycles. In the case of the BVC electrode, we observed CRs of 80.34% (actual), 80.26% (predicted), and 79.58% (forecasted) and CEs of 99.33% (actual), 99.37% (predicted), and 98.87% (forecasted), as depicted in Figure 7E. However, the BVC electrode showed CRs of 94.78%

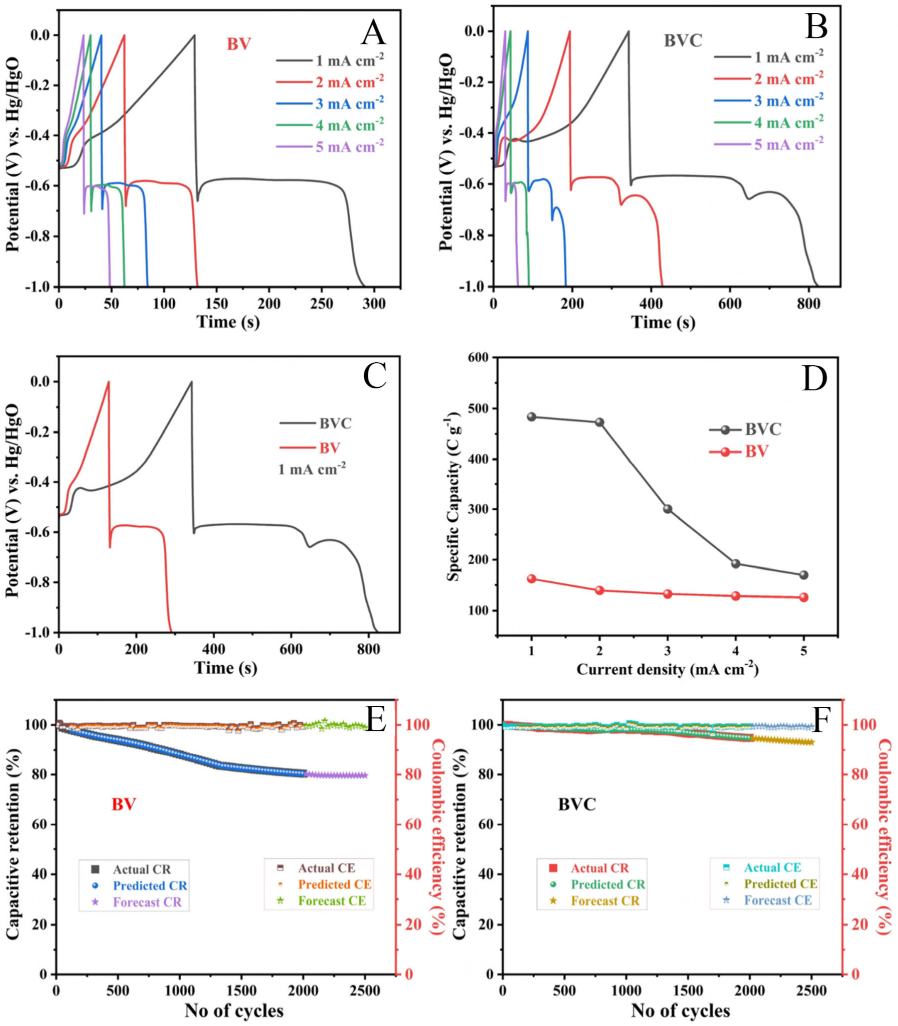

Figure 7. (A and B) GCD curves at different current densities for BV and BVC electrodes; (C) Comparative GCD curves of corresponding electrodes at 1 mA cm^{-2} current density; (D) Plots of current density *vs.* specific capacity; (E and F) Actual, predicted, and forecast capacitive retention and Coulombic efficiency of BV and BVC electrodes. BV: $BiVO_4$; BVC: bismuth vanadate/carbon; GCD: galvanostatic charge discharge.

(actual), 94.64% (predicted), and 92.99% (forecasted) and CEs of 99.37% (actual), 99.35% (predicted), and 99.29% (forecasted), as shown in Figure 7F. The stability implies that the carbon present in the sample can stabilize to a great extent.

Aqueous symmetric supercapacitor device study

Based on the excellent performance of BVC electrodes, the practical and commercial applicability of BVC was also tested by fabricating and testing the aqueous and solid-state type of symmetric SC (SSc).

The aqueous symmetric SC (ASc) device is fabricated and the steps in fabrication are provided in Supplementary Figure 4 where the BVC electrode acts as an anode and cathode in 1M KOH electrolyte. For improved SSc performance, it is important to attain the equilibrium of charge between the electrodes using the relationship q+ = q-, where q+ is the charge stored on the surface of the positive and q- is the charge stored on the negative electrode. The important parameters strongly influence the specific capacitance (SC), potential (ΔV) and the mass of the electrode material (m). The mass on the cathode and anode is balanced

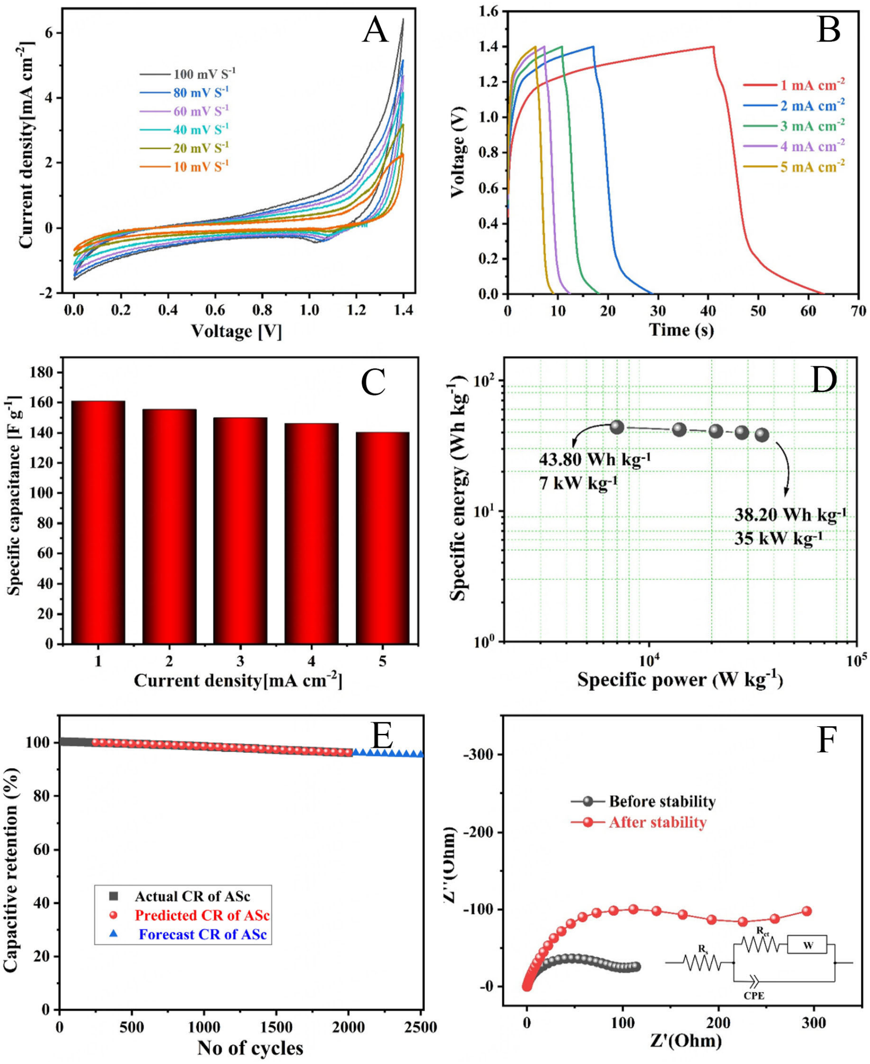

Figure 8. (A) CV curves at different current densities for BVC aqueous symmetric supercapacitor (ASc) device; (B) GCD curves of the ASc device; (C) Bar diagram for specific capacitance at various current densities; (D) Ragone plots of specific energy and specific power; (E) Actual, predicted, and forecast capacitive retention for 2000 cycles; (F) EIS Nyquist plots of before and after stability of the ASc device. BVC: Bismuth vanadate/carbon; CV: cyclic voltammetry; GCD: galvanostatic charge discharge; EIS: electrochemical impedance spectroscopy.

and the performance ASc is measured in 1M KOH electrolyte by taking the CV from 0 V to 1.4 V voltage window. The CV curves of the ASc device are recorded at various scan rates (10 mV s^{-1} to 100 mV s^{-1}), as represented in Figure 8A. The shape of CV indicates that high current density does not cause distortion on the electrode, indicating the stability of BVC material at 100 mV s^{-1}. This finding emphasizes the rate capabilities of an ASc device, exhibiting its ability to maintain high scan rates while remaining highly reversible.

The GCD measurements of the fabricated ASc device were also recorded at 1 to 5 mA cm^{-2} current densities at 0 V to 1.4 V voltage window represented in Figure 8B. The pseudocapacitive behavior can be observed and the SC was evaluated from the GCD curves with the highest SCs of 160.9 F g^{-1} at 1 mA cm^{-2} current density using Supplementary Equation 17. The SC of the device from GCD curves from 1 mA cm^{-2} to 5 mA cm^{-2} current densities is depicted in Figure 8C. The SE and SP of the ASc device are calculated from

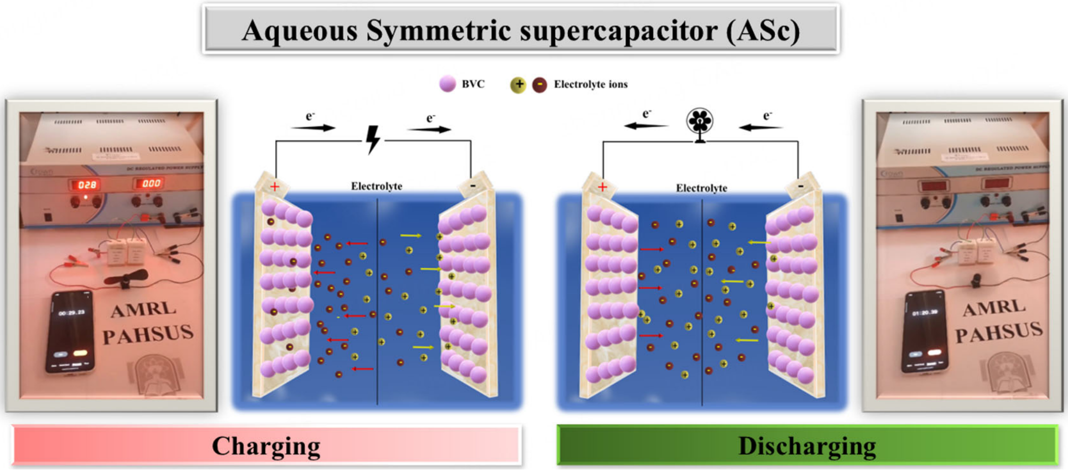

Figure 9. Photographs of the practical application of rotating the fan using the ASc device of BVC in charging and discharging mode. ASc: Aqueous symmetric supercapacitor; BVC: bismuth vanadate/carbon.

Supplementary Equations 18 and 19 and are represented in the Ragone plot [Figure 8D]. The device exhibits a high SE of 43.80 Wh kg^{-1} at a SP of 7 kW kg^{-1} and remains at 38.20 Wh kg^{-1} SE at a SP of 35 kW kg^{-1}. The SE and SP of the device are compared with literature values and are shown in the Ragone plot [Supplementary Figure 5]. The stability and long-term durability of the device are also important aspects of its performance. The cyclic stability was evaluated at 5 mA cm^{-2}, with the CR of ASc for 2000 cycles and a CE of 85.71%. The observed CRs of 96.25% (actual), 96.28 % (predicted), and 95.42 % (forecasted) for the next 500 cycles are represented in Figure 8E. Supplementary Equations 20 and 21 are used to calculate CR and CE. This measurement highlights the potential of ASc as a high-performance electrochemical energy storage device. The EIS measurements before and after the stability of the device are depicted in Figure 8F. The equivalent circuit model used to fit the Nyquist EIS plots and the circuit parameters are represented in Supplementary Table 5.

The ASc device is further used for actual practical applications to demonstrate the capability of the material to store and rapidly release energy by rotating a mini fan with two leaves. This application gives the materials SE, SP, and discharge behavior. The demonstration of fan rotation is shown in Figure 9 and in Supplementary Video 2. The device is charged at 2.8V for 30 s as the two devices are connected in series and it takes 54 s to discharge by rotating the leaf of a fan.

Soid-state symmetric supercapacitor device study

The performance of ASc is promising. To support these results, a solid-state SSc is also constructed; as compared to aqueous electrolyte-based devices, solid-state devices offer an extensive range of applications due to advantages such as easy handling, no spillage, and great performance consistency. SSc was fabricated using BVC as both the anode and cathode material on a 5 × 5 cm^2 SS sheet. The fabrication process is provided in Supplementary Section 1.3, with polyvinyl alcohol in 1 M KOH (PVA-KOH) as the gel electrolyte. The preparation of the gel electrolyte is described in Supplementary Section 1.4. The electrochemical performance of the device is tested within a 0 V to 1.4 V voltage window, similar to ASc, after optimizing the voltage range from 1.2 V to 1.6 V at a 50 mV s^{-1} scan rate. The CV analysis is performed at various scan rates (10 mV s^{-1} to 100 mV s^{-1}) within a 0 V to 1.4 V voltage window, yielding a perfectly symmetrical shape, as depicted in Figure 10A, which indicates the accurate mass and charge balance between the electrodes.

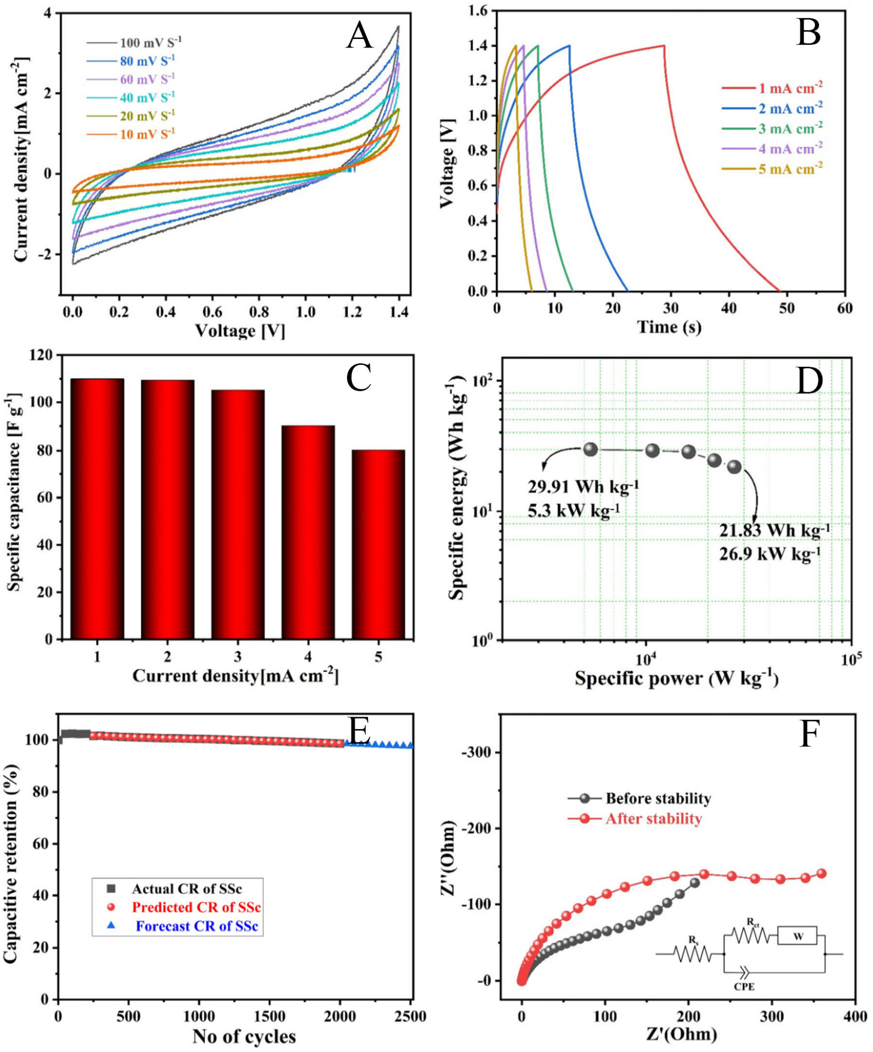

Figure 10. (A) CV curves at different current densities for BVC Solid-state symmetric supercapacitor (SSc) device; (B) GCD curves of the SSc device; (C) Bar diagram for specific capacitance at various current densities; (D) Ragone plots of specific energy and specific power; (E) Actual, predicted, and forecast capacitive retention for 2000 cycles; (F) EIS Nyquist plots of before and after stability of the SSc device. BVC: Bismuth vanadate/carbon; CV: cyclic voltammetry; GCD: galvanostatic charge discharge; EIS: electrochemical impedance spectroscopy.

The GCD analysis was used to evaluate the SCs of the device and the recorded GCD from 1 to 5 mA cm^{-2} current densities at 0 V to 1.4 V voltage window plotted in Figure 10B. The symmetrical charge and discharge curve indicated the steady charge transfer during charging and discharging. The obtained SC of the device is 109.8 F g^{-1} at 1 mA cm^{-2} current density [Figure 10C]. The Specific Energy (SE) and Specific Power (SP) of the SSc device are calculated and plotted in the Ragone plot Figure 10D. The device exhibits a high SE of 29.91 Wh kg^{-1} SE at a 5.3 kW kg^{-1} SP, which remains at 21.83 Wh kg^{-1} SE at a 26.9 kW kg^{-1}. The SE and SP of the device are compared with literature values and shown in the Ragone plot [Supplementary Figure 5]. The Ragone plot indicates that this material showed excellent SP and SE when compared to existing literature. The cyclic stability of the fabricated SSc was investigated for 2000 charging-discharging cycles at 5 mA cm^{-2} with 86.36% CE. The observed CRs of 98.62% (actual), 98.64% (predicted), and 97.56% (forecasted) for the next 500 cycles are depicted in Figure 10E. The EIS measurements of before and after cyclic stability of the SSc are represented in Figure 10F. The circuit parameters are represented in

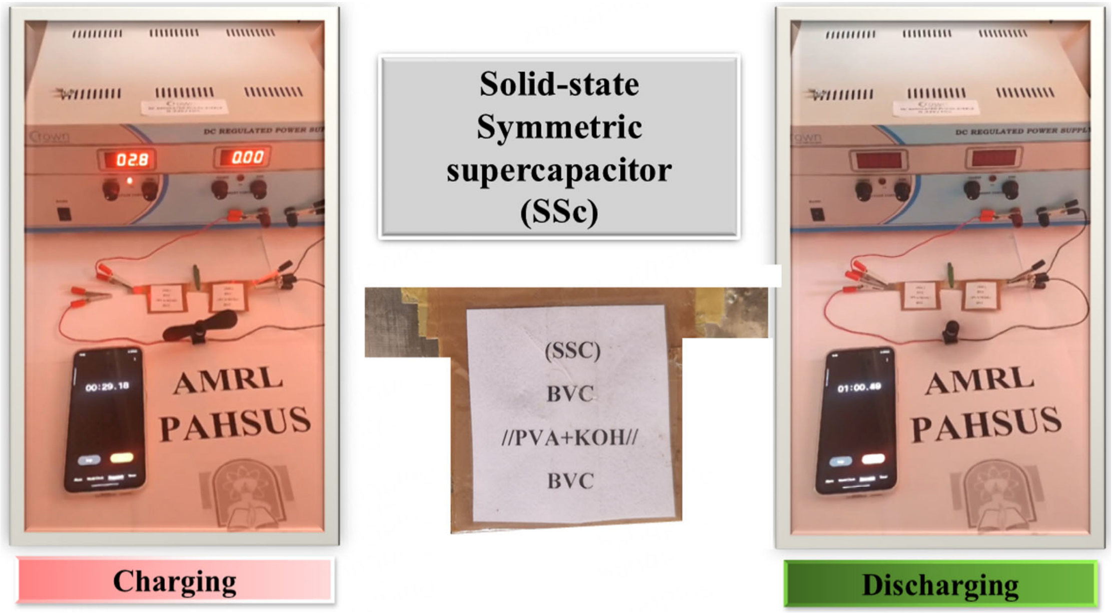

Figure 11. Photographs of the practical application of rotating the fan using the SSc device of BVC in charging and discharging mode. BVC: Bismuth vanadate/carbon; SSc: solid-state symmetric supercapacitor.

Supplementary Table 5.

Similar to the ASc device, the SSc is used in practical applications by rotating a fan to record discharge behavior, as shown in Figure 11 and in Supplementary Video 3. The device is charged at 2.8 V for 30 s while the two devices are connected in series, and it discharges by rotating the fan for 33 s.

Overall, the conductivity of the BV nanoparticles, doped with adventitious carbon and synthesized through a simple and efficient MOF-derived approach, exhibited exceptional performance in OER and SC applications within flexible ASc and SSc devices. This remarkable performance can be attributed to several factors: (i) the successful incorporation of an optimal amount of sp^2 hybridized carbon into the BV matrix, resulting in improved electronic conductivity; (ii) the uniform distribution of coral-like BV nanoparticles with diminished particle size and elevated R_F values, which significantly reduce the charge-carrier diffusion length by generating oxygen vacancies; (iii) an enhanced electrochemically active surface area, as indicated by increased C_{dl} and ECSA values; and (iv) lower EIS values (R_s and R_{ct}), which facilitate effective interactions between the working electrode material and the electrolyte. Furthermore, the LSTM-based machine learning approach effectively models, predicts, and forecasts the OER and supercapacitive performance of BVC electrodes.

CONCLUSIONS

In summary, we demonstrated a new approach to synthesize multifunctional MOF-derived BV/carbon composite using monometallic Bi and V MOFs via solid-state grinding and high-temperature pyrolysis. The well-characterized samples were then utilized to test the multifunctional behavior of the as-prepared samples toward electrochemical OER and SC applications. The BVC sample showed exceptional performance for OER with an overpotential of 364 mV at the current density of 10 mA cm^{-2} and the SC has a high specific capacity of 134.17 mAh g^{-1} (483 C g^{-1}) at 1 mA cm^{-2} current density. The constructed ASc device shows a SC of 160.9 F g^{-1} at a current density of 1 mA cm^{-2} and excellent stability with a CR of

96.25%. Similarly, the SSc device shows a SC of 109.8 F g^{-1} at a 1 mA cm^{-2} current density along with a 98.62% CR. The LSTM-based machine learning technique successfully models, predicts, and forecasts the chronoamperometric stability of MOF-derived BVC electrodes and CR and CE of BV and BVC electrodes. The as-designed aqueous and solid-state devices have been successfully applied to rotate a two-blade fan. The excellent performance of BVC indicates its enhanced physicochemical properties due to carbon doping. This synthesis method for bimetallic MOFs has opened up new pathways for creating similar materials for multifunctional applications.

DECLARATIONS

Author's contributions

Writing - original draft, methodology, investigation, conceptualization: Chaudhari, S. A.
Writing - review and editing, formal analysis: Patil, V. V.
Investigation, data curation: Jadhav, V. A.
Data curation, formal analysis: Thorat, P.
Data curation, formal analysis: Sutar, S. S.
Writing - review and editing, data curation, formal analysis: Dongale, T. D.
Writing - review and editing, data curation: Parale, V.
Formal analysis: Patil, V.
Writing - review and editing, supervision, conceptualization: Mhamane, D. S.
Writing - review and editing, supervision, funding acquisition, conceptualization: Mali, M. G.
Writing - review and editing, supervision, funding acquisition, conceptualization: Park, H. H.
All authors reviewed the results and approved the final manuscript version.

Availability of data and materials

The rata data supporting the findings of this study are available within this Article and its Supplementary Materials. Further data are available from the corresponding authors upon request.

Financial support and sponsorship

Funding for this work was provided through the Brain Pool Program supported by the Ministry of Science and ICT via the National Research Foundation of Korea (Grant No: RS-2024-00444441). This work was supported by the National Research Foundation of Korea (NRF), funded by the Korea government (MSIT) (RS-2020-NR049541). Author Chaudhari, S. A. acknowledges the Mahatma Jyotiba Phule Research and Training Institute (MAHAJYOTI), Nagpur (An Autonomous Institute of the Other Backward Class Bahujan Welfare Department, Government of Maharashtra), for awarding the MAHAJYOTI FELLOW honor and offering financial support under the Mahatma Jyotiba Phule Research Fellowship-2022 (MAHAJYOTI2022/Ph.D. Fellow/ 1002(829).

Conflicts of interest

All authors declared that there are no conflicts of interest.

Ethical approval and consent to participate

Not applicable.

Consent for publication

Not applicable.

Copyright

REFERENCES

1. Patil, V. V.; Pujari, S. S.; Bhosale, S. B.; et al. Hydrous and amorphous cobalt phosphate thin-film electrodes synthesized by the SILAR method for high-performing flexible hybrid energy storage devices. *Energy. Fuels.* **2022**, *36*, 12791-806. DOI
2. Reddy, C. V.; Reddy, I. N.; Ravindranadh, K.; et al. Effect of noble metal ions dopants on solar photoelectrochemical water splitting and electrochemical supercapacitive performance of $BiVO_4$ hollow tubes. *Sol. Energy. Mater. Sol. Cells.* **2021**, *226*, 111056. DOI
3. Ismail KB, Arun Kumar M, Jayavel R, Arivanandhan M, Mohamed Ismail MA. Enhanced electrochemical performance of the MoS_2/Bi_2S_3 nanocomposite-based electrode material prepared by a hydrothermal method for supercapacitor applications. *RSC. Adv.* **2023**, *13*, 24272-85. DOI
4. Jiao, S.; Zhou, A.; Wu, M.; Hu, H. Kirigami patterning of MXene/bacterial cellulose composite paper for all-solid-state stretchable micro-supercapacitor arrays. *Adv. Sci.* **2019**, *6*, 1900529. DOI PubMed PMC
5. Liu, H.; Liu, X.; Wang, S.; Liu, H.; Li, L. Transition metal based battery-type electrodes in hybrid supercapacitors: a review. *Energy. Storage. Mater.* **2020**, *28*, 122-45. DOI
6. Dubal, D. P.; Patil, D. R.; Patil, S. S.; Munirathnam, N. R.; Gomez-Romero, P. $BiVO_4$ fern architectures: a competitive anode for lithium-ion batteries. *ChemSusChem* **2017**, *10*, 4163-9. DOI PubMed
7. Devi, N.; Ray, S. S. Performance of bismuth-based materials for supercapacitor applications: a review. *Mater. Today. Commun.* **2020**, *25*, 101691. DOI
8. Shinde, N. M.; Shinde, P. V.; Mane, R. S.; Ho, K. K. Solution-method processed Bi-type nanoelectrode materials for supercapacitor applications: a review. *Renew. Sustainable. Energy. Rev.* **2021**, *135*, 110084. DOI
9. Cao, Z.; Fu, J.; Wu, M.; Hua, T.; Hu, H. Synchronously manipulating Zn^{2+} transfer and hydrogen/oxygen evolution kinetics in MXene host electrodes toward symmetric Zn-ions micro-supercapacitor with enhanced areal energy density. *Energy. Storage. Mater.* **2021**, *40*, 10-21. DOI
10. Isacfranklin, M.; Deepika, C.; Ravi, G.; Yuvakkumar, R.; Velauthapillai, D.; Saravanakumar, B. Nickel, bismuth, and cobalt vanadium oxides for supercapacitor applications. *Ceram. Int.* **2020**, *46*, 28206-10. DOI
11. Patil, S. S.; Dubal, D. P.; Tamboli, M. S.; et al. Ag:$BiVO_4$ dendritic hybrid-architecture for high energy density symmetric supercapacitors. *J. Mater. Chem. A.* **2016**, *4*, 7580-4. DOI
12. Deeloed, W.; Priamushko, T.; Čížek, J.; Suramitr, S.; Kleitz, F. Defect-engineered hydroxylated mesoporous spinel oxides as bifunctional electrocatalysts for oxygen reduction and evolution reactions. *ACS. Appl. Mater. Interfaces.* **2022**, *14*, 23307-21. DOI PubMed PMC
13. Xie, X.; Du, L.; Yan, L.; et al. Oxygen evolution reaction in alkaline environment: material challenges and solutions. *Adv. Funct. Mater.* **2022**, *32*, 2110036. DOI
14. Heckel, S.; Wittmann, M.; Reid, M.; Villa, K.; Simmchen, J. An account on $BiVO_4$ as photocatalytic active matter. *Acc. Mater. Res.* **2024**, *5*, 400-12. DOI PubMed PMC
15. Kubba, D.; Ahmed, I.; Kour, P.; et al. $LaCoO_3$ perovskite nanoparticles embedded in $NiCo_2O_4$ nanoflowers as electrocatalysts for oxygen evolution. *ACS. Appl. Nano. Mater.* **2022**, *5*, 16344-53. DOI
16. Shen, M.; Ma, H. Metal-organic frameworks (MOFs) and their derivative as electrode materials for lithium-ion batteries. *Coord. Chem. Rev.* **2022**, *470*, 214715. DOI
17. Lin, W.; Zhao, S.; Lu, B.; Jiang, F.; Lu, Z.; Xu, Z. Structures, performances and applications of green biomass derived carbon in lithium-ion batteries. *Energy. Mater.* **2024**, *4*, 400078. DOI
18. Chettiannan, B.; Dhandapani, E.; Arumugam, G.; Rajendran, R.; Selvaraj, M. Metal-organic frameworks: a comprehensive review on common approaches to enhance the energy storage capacity in supercapacitor. *Coord. Chem. Rev.* **2024**, *518*, 216048. DOI
19. Li, J.; Jia, J.; Wang, D.; Dong, H.; Zhu, M. Recent research progress of MOFs-based heterostructures for photocatalytic hydrogen evolution. *Chem. Eng. J.* **2024**, *498*, 155194. DOI
20. Qi, Q.; Zhang, C.; Hu, J. Triggered factors and structure-activity relationship in the dynamic reconstruction processing of MOF for the alkaline oxygen evolution reaction. *Coord. Chem. Rev.* **2025**, *522*, 216235. DOI
21. Khan, M. S.; Li, Y.; Yang, L.; et al. Improving capacitive deionization performance through tailored iodine-loaded ZIF-8 composites. *Desalination* **2024**, *579*, 117486. DOI
22. Li, S.; Gao, Y.; Li, N.; Ge, L.; Bu, X.; Feng, P. Transition metal-based bimetallic MOFs and MOF-derived catalysts for electrochemical oxygen evolution reaction. *Energy. Environ. Sci.* **2021**, *14*, 1897-927. DOI
23. Du, J.; Li, F.; Sun, L. Metal-organic frameworks and their derivatives as electrocatalysts for the oxygen evolution reaction. *Chem. Soc. Rev.* **2021**, *50*, 2663-95. DOI
24. Zhu, Z.; Duan, J.; Chen, S. Metal-organic framework (MOF)-based clean energy conversion: recent advances in unlocking its underlying mechanisms. *Small* **2024**, *20*, 2309119. DOI PubMed
25. Reddy C, Neelakanta Reddy I, Koutavarapu R, Reddy KR, Kim D, Shim J. Novel $BiVO_4$ nanostructures for environmental remediation, enhanced photoelectrocatalytic water oxidation and electrochemical energy storage performance. *Solar. Energy.* **2020**, *207*, 441-9. DOI

26. Chaudhari, S.; Patil, V.; Jadhav, V.; et al. Linker encouraged solid state synthesis of MOF derived Z-scheme $NiCo_2O_4$/NiO/C toward efficient removal of organic and inorganic pollutants from water. *Langmuir* **2024**, *40*, 19804-15. DOI
27. Sonkawade, A. R.; Mahajan, S. S.; Shelake, A. R.; et al. The g-C_3N_4/rGO composite for high-performance supercapacitor: synthesis, characterizations, and time series modeling and predictions. *Int. J. Hydrogen. Energy.* **2024**, *87*, 1416-26. DOI
28. Kolhe, N. D.; Walekar, L. S.; Kadam, A. N.; et al. MOF derived in-situ construction of core-shell Z-scheme $BiVO_4$@ -Fe_2O_3-CF nanocomposites for efficient photocatalytic treatment of organic pollutants under visible light. *J. Clean. Prod.* **2023**, *420*, 138179. DOI
29. Packiaraj, R.; Venkatesh, K.; Devendran, P.; Bahadur, S. A.; Nallamuthu, N. Structural, morphological and electrochemical studies of nanostructured $BiVO_4$ for supercapacitor application. *Mater. Sci. Semicond. Process.* **2020**, *115*, 105122. DOI
30. Mathad, S. N.; Jadhav, R. N.; Patil, N. D.; Puri, V. Structural and mechanical properties of Sr^{+2}-doped bismuth manganite thick films. *Int. J. Self-Propag. High-Temp. Synth.* **2013**, *22*, 180-4. DOI
31. Orimolade, B. O.; Arotiba, O. A. An exfoliated graphite-bismuth vanadate composite photoanode for the photoelectrochemical degradation of acid orange 7 dye. *Electrocatalysis* **2019**, *10*, 429-35. DOI
32. Samsudin, M. F. R.; Jayabalan, P. J.; Ong, W.; Ng, Y. H.; Sufian, S. Photocatalytic degradation of real industrial poultry wastewater via platinum decorated $BiVO_4$/g-C_3N_4 photocatalyst under solar light irradiation. *J. Photochem. Photobiol. A. Chem.* **2019**, *378*, 46-56. DOI
33. Biswas, M. R. U. D.; Ho, B. S.; Oh, W. Eco-friendly conductive polymer-based nanocomposites, $BiVO_4$/graphene oxide/polyaniline for excellent photocatalytic performance. *Polym. Bull.* **2020**, *77*, 4381-400. DOI
34. Sajid, M. M.; Khan, S. B.; Javed, Y.; et al. Facile synthesis of Se/$BiVO_4$ heterojunction composite and evaluation of synergetic reaction mechanism for efficient photocatalytic staining of organic dye pollutants in wastewater under visible light. *J. Mater. Sci. Mater. Electron.* **2020**, *31*, 19599-612. DOI
35. Phanichphant, S.; Nakaruk, A.; Chansaenpak, K.; Channei, D. Evaluating the photocatalytic efficiency of the $BiVO_4$/rGO photocatalyst. *Sci. Rep.* **2019**, *9*, 16091. DOI PubMed PMC
36. Patil, V. V.; Kumar, N.; Salunkhe, R. R.; et al. Crystallinity transformation engineering of hydrous cobalt nickel phosphate cathodes for hybrid supercapacitor devices: extrinsic/battery to intercalation type pseudocapacitors. *Chem. Eng. J.* **2024**, *485*, 150055. DOI
37. Subramanyam, P.; Khan, T.; Neeraja, S. G.; Suryakala, D.; Subrahmanyam, C. Plasmonic Bi nanoparticle decorated $BiVO_4$/rGO as an efficient photoanode for photoelectrochemical water splitting. *Int. J. Hydrogen. Energy.* **2020**, *45*, 7779-87. DOI
38. Patil, S. S.; Dubal, D. P.; Deonikar, V. G.; et al. Fern-like rGO/$BiVO_4$ hybrid nanostructures for high-energy symmetric supercapacitor. *ACS. Appl. Mater. Interfaces.* **2016**, *8*, 31602-10. DOI
39. Biesinger, M. C. Accessing the robustness of adventitious carbon for charge referencing (correction) purposes in XPS analysis: insights from a multi-user facility data review. *Appl. Surf. Sci.* **2022**, *597*, 153681. DOI
40. Wu, J.; Chen, Y.; Pan, L.; et al. Multi-layer monoclinic $BiVO_4$ with oxygen vacancies and V^{4+} species for highly efficient visible-light photoelectrochemical applications. *Appl. Catal. B. Environ.* **2018**, *221*, 187-95. DOI
41. Guo, M.; Wang, Y.; He, Q.; et al. Enhanced photocatalytic activity of S-doped $BiVO_4$ photocatalysts. *RSC. Adv.* **2015**, *5*, 58633-9. DOI
42. Nguyen, T. D.; Bui, Q. T. P.; Le, T. B.; et al. Co^{2+} substituted for Bi^{3+} in $BiVO_4$ and its enhanced photocatalytic activity under visible LED light irradiation. *RSC. Adv.* **2019**, *9*, 23526-34. DOI
43. Mir, R. A.; Pandey, O. P. Role of morphological features and oxygen vacancies on electrocatalytic oxygen evolution reaction (OER) activity and pseudocapacitance performance of $BiVO_4$ structures. *Appl. Phys. Lett.* **2021**, *118*, 253902. DOI
44. Patil, V. V.; Pujari, S. S.; Bhosale, S. B.; et al. SILAR synthesized binder-free, hydrous cobalt phosphate thin film electrocatalysts for OER application: annealing effect on the electrocatalytic activity. *Int. J. Energy. Res.* **2023**, *2023*, 5570480. DOI
45. Arora, Y.; Shah, A. P.; Battu, S.; et al. Nanostructured MoS_2/$BiVO_4$ composites for energy storage applications. *Sci. Rep.* **2016**, *6*, 36294. DOI PubMed PMC